High resolution, high efficiency liquid scintillator capillary array for gamma imaging

Mei Zhang, Huasi Hu, Kuinian Li, Bodong Peng, Liang Sheng, Dongwei Hei, and Yang Li

Citation: Review of Scientific Instruments **89**, 073506 (2018); doi: 10.1063/1.5026131
View online: https://doi.org/10.1063/1.5026131
View Table of Contents: http://aip.scitation.org/toc/rsi/89/7
Published by the American Institute of Physics

High resolution, high efficiency liquid scintillator capillary array for gamma imaging

Mei Zhang,[1,2] Huasi Hu,[1,a)] Kuinian Li,[2] Bodong Peng,[2] Liang Sheng,[2] Dongwei Hei,[2] and Yang Li[2]
[1]*School of Energy and Power Engineering, Xi'an Jiaotong University, Xi'an 710049, China*
[2]*State Key Laboratory of Intense Pulsed Radiation Simulation and Effect, Northwest Institute of Nuclear Technology, Xi'an 710024, China*

(Received 15 February 2018; accepted 8 July 2018; published online 30 July 2018)

We fabricated a liquid scintillator capillary array (LSCA) for gamma imaging with the aim of developing a one-dimensional detector system utilizing a streak camera for high temporal and spatial resolution pulsed gamma radiation detection. The detector's performance was studied in a simulation and via an experiment. The maximum efficiency of the LSCA's emission was at a wavelength of 420 nm. To establish a high fidelity representation of the detector's edge spread function and modulation transfer function (MTF), a slanted edge algorithm was introduced to calculate the edge spread function of the discrete sampling array's image screen. The simulation results showed that the spatial resolution of the LSCA was better for 14 MeV neutrons than for 1.25 MeV gamma radiation. The experimental results show that in comparison with a 6-mm-thick $LaBr_3$ image plate, the LSCA had a higher temporal and spatial resolution when used as a gamma detector. The spatial resolution was 1.1 lp/mm (MTF = 0.1) for the LSCA. In addition, when an ultra-violet streak camera was coupled with the LSCA, it had a comparable sensitivity to that of a 6-mm-thick $LaBr_3$ image plate. *Published by AIP Publishing.*
https://doi.org/10.1063/1.5026131

I. INTRODUCTION

Gamma imaging is being adopted in the fields of security, astronomy, medical imaging, and diagnosis in the form of pulsed radiation facilities.[1–3] Scintillators are used to convert gamma radiation into flashes of light that can be transmitted and recorded easily. For gamma imaging plates, it is important to have a high density, short decay time, excellent spatial resolution, and ability to manufacture large plates. Over the last 20 yrs, many Ce^{3+} activated scintillators have been developed. Lu_2SiO_5:Ce detectors combine a high density with a fast scintillation response and are used in scanners for medical diagnostics.[4] The newest scintillators $LaCl_3$:10%Ce and $LaBr_3$:5%Ce^{3+} were discovered at Delft University and provide record high energy resolution and ultrafast detection of gamma rays. While $LaBr_3$ scintillators have excellent gamma imaging properties, their size is limited to below 10 cm because of crystal growth issues and its decay time is about 20 ns, which is too long for some applications such as detection involving short pulse gamma radiation sources with pulses of a several tens of nanoseconds in duration.[5,6] One approach for solving these issues is to use scintillating fiber arrays. Scintillating fibers allow for a high resolution via a thicker detector that increases the quantum efficiency without substantially degrading the imaging resolution.[7] The spatial resolution of a scintillating fiber for gamma detection depends on the diameter and the spread of secondary particles, i.e., protons or electrons. Based on theoretical simulations and experimental results, the spatial resolution can be improved by decreasing the fiber diameter.[8] We measured the modulation transfer function (MTF) of scintillating fiber arrays with single fiber diameters (equivalent to pixels) of 0.3 and 0.5 mm. The results show that the spatial resolution of an array with pixel diameters of 0.3 mm was below 1 lp/mm, at only 0.8 lp/mm (MTF = 0.1) and that of a 0.5 mm pixel diameter array was lower, at about 0.6 lp/mm. Additionally, the scintillating fiber arrays with the larger pixels (e.g., 0.3-mm-diameter and 0.5-mm-diameter pixels) had a poor uniformity and showed significant distortion and dislocation effects. Efforts are thus underway in the research community to develop a one-dimensional, high temporal–spatial resolution detection device that is composed of a scintillating image plate and a streak camera for pulsed gamma radiation detection. Our research team has focused on the study of scintillating fiber arrays with smaller pixel cross sections to achieve higher spatial resolutions and good uniformity. However, the size of single scintillating fibers ranged from 0.25 to 5 mm square or round cross sections in the France's Saint-Gobain scintillation product guides. Liquid scintillator capillary arrays have been reported for imaging 14 MeV neutrons.[8–10] Thus, we began to develop a liquid scintillator capillary array (LSCA) and studied its performance for gamma radiation imaging.

In this paper, some of the LSCA's characteristics, such as its emission spectrum, spatial resolution, and relative sensitivity, are reported and compared with those of a $LaBr_3$ image plate.

II. EMISSION SPECTRUM OF THE LSCA

The left panel in Fig. 1 shows a photograph of the LSCA. The large coherent array was made up of 100-μm-diameter,

a)Author to whom correspondence should be addressed: huasi_hu@xjtu.edu.cn

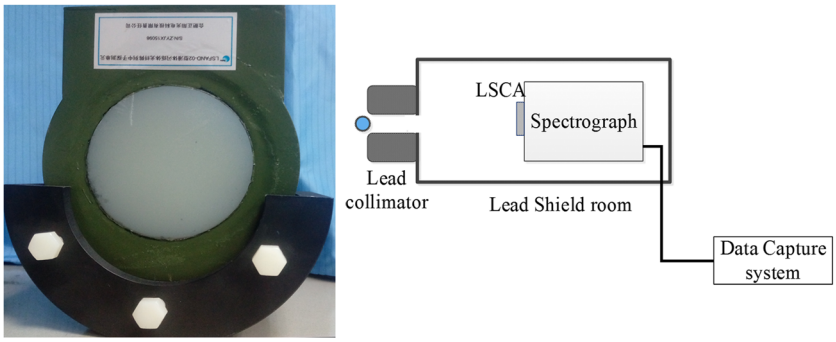

FIG. 1. A photograph of the LSCA (left) and a sketch of the setup to measure the emission spectrum (right).

60-mm-long glass capillaries filled with an EJ309 liquid scintillator (made by ELJEN Technology, USA). EJ309 is a fast-response scintillator with a decay time of 3.5 ns. The thickness of the glass capillary wall was 0.02 mm. The active imaging area of the array was 80 mm in diameter. Both ends of the capillary array were enclosed by a fiber optic faceplate so that both surfaces can be used for imaging simultaneously. Its emission spectrum was measured at a unique hard X-ray source facility. The X-ray tube voltage was set at 60 kV, and the tube current was 50 mA. A sketch of the experimental setup is shown in the right panel of Fig. 1. The measurement result is given in Fig. 2. In Fig. 2, the spectral range spans from 360 to 500 nm and the maximum emission peak is located at a wavelength of 426 nm. In comparison with the $LaBr_3$ image plate, most image detectors have a higher efficiency in this wavelength range. The emission spectrum of $LaBr_3$ can vary with the concentration of Ce^{3+}, and its maximum emission wavelength is around 350–380 nm.

III. SPATIAL FREQUENCY RESPONSE OF THE LSCA

A. Calculation of the modulation transfer function

The modulation transfer function (MTF) is a fundamental imaging system design specification and system quality metric. It describes the spatial frequency response of an image forming system and can be obtained through an edge spread function (ESF) using the following equations:[15]

$$LSF(x) = \frac{\mathrm{d}}{\mathrm{d}x}(ESF(x)), \tag{1}$$

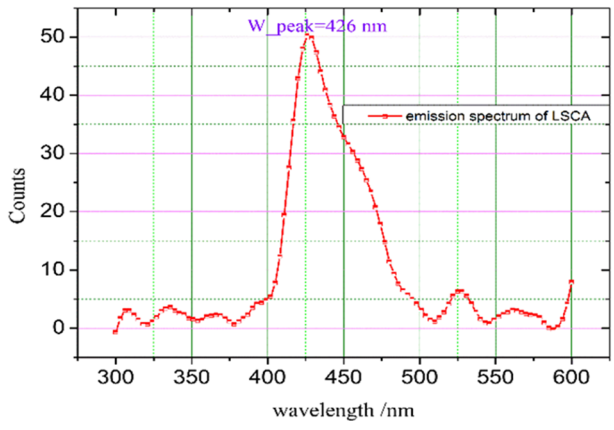

FIG. 2. Experimentally measured emission spectrum of the LSCA.

$$MTF(f) = F(LSF(x)). \tag{2}$$

In Eq. (2), F is the Fourier transform operator.

To date, most techniques for measuring the MTFs of image detectors have involved imaging bar targets, sinusoidal targets, or knife edges. These deterministic methods were originally used for measuring the MTFs of continuous imaging systems. When image detectors with discrete elements sample the image of a target, the output depends on the phase of the target image with respect to the structure of the sampling array.[11–14] Owing to the deep penetration and strong scattering of gamma radiation or neutrons, the sampling edge of a bar target is a more appropriate method for measuring the MTF. To precisely evaluate the spatial resolution of the LSCA, a sloping edge was used for the bar target. For a sloping edge image, the ESF of a discrete sample can be deduced through the geometry shown in Fig. 3(a) and can be expressed as follows:[15,16]

$$ESF(k) = \frac{\sum_{i=0}^{M-1}\sum_{j=0}^{N-1} f(i,j)\delta(k-k_i-\mathrm{j})}{\sum_{i=0}^{M-1}\sum_{j=0}^{N-1}\delta(k-k_i-\mathrm{j})}, \tag{3}$$

where $f(i, j)$ is a two-dimensional discrete digital image of $M \times N$ pixels (i and j are the positions of the coordinate axis in the horizontal and vertical direction, respectively), while k is the position on the coordinate axis perpendicular to the edge. As Fig. 3(b) shows, $ESF(k)$ is composed of the segments of the projections of each row of $f(i, j)$; those overlapping segments should be averaged. $ESF(k)$ can be calculated via the iteration method.[15,16] The iteration formula is expressed by the following equation:

$$ESF^{(0)}(k) = f(0,\mathrm{j}), j = k, k \in [0, N-1],$$

$$ESF^{(i)}(k) = \begin{cases} ESF^{(i-1)}(k), k \in [0, k_i - 1] \\ [ESF^{(i-1)}(k) + f(i, k-k_i)]/2, k \in [k_i, k_{i-1} + N - 1] \\ f(i, k-k_i), k \in [k_i + N - 1, k_{i-1} + N] \end{cases}. \tag{4}$$

B. Simulation of the ESF

Simulations of the ESF of LSCA were performed by using the MCNPX code. Figure 4 shows the simulation model—its geometry is the same as that depicted in Sec. II. In Fig. 4, the source is specified as a rectangular plane source and consists

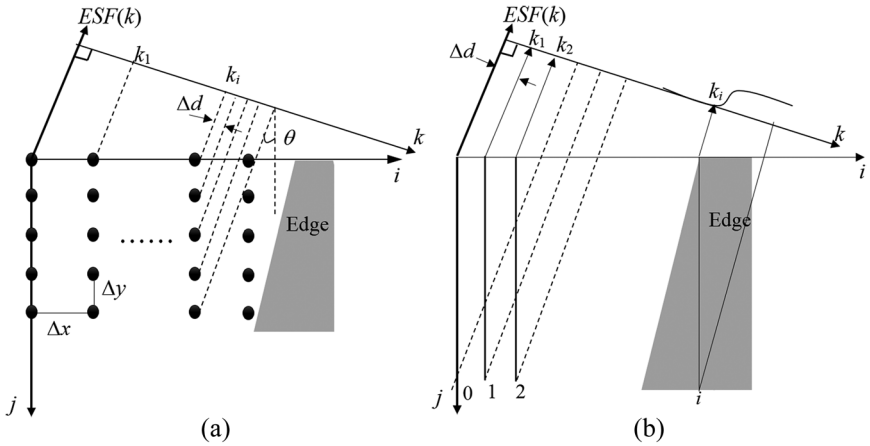

FIG. 3. (a) Projection diagram of the edge image for the ESF and (b) an illustration of how the ESF is calculated.

of an ideal, non-divergent, and parallel particle beam. The spatial distribution of emitted particles (gammas or neutrons) is uniform in this plane. In accordance with the above-described principle for measuring the MTF of an array consisting of discrete elements, the angle of the slope of the plane source relative to the horizontal direction of the array was designed to be 6°, as shown in Fig. 4. The angle of the slope was chosen so that along the upper edge of the rectangular plane the first capillary in every 10 capillaries is not irradiated and the last one is fully irradiated. In the MCNPX code, the 1.25 MeV gammas and 14 MeV neutrons were, respectively, set as the source particles. The output of the simulation yielded the deposited energy spectrum of the secondary particles (protons or electrons) in each capillary. The total output of the luminescence in each capillary can be calculated according to the deposited energy and the light response of the EJ309 scintillator. Figure 5 shows the ESF image simulated for 1.25 MeV gamma radiation.

The amount of light created in the irradiated capillary was determined from the deposited energy from protons or electrons adjacent to the interaction spot. Light in the neighboring capillaries is created by protons or electrons crossing over from the radiated capillary to its neighbors and by scattered neutrons or gamma radiation. By adding up the total amount of light in all fifteen capillaries along the direction perpendicular to the edge of the ESF image, the amount of scintillation light in each capillary could be determined; it is plotted in the left panel of Fig. 6—every pixel on the horizontal axis represents a capillary. For 14 MeV neutrons, the amount of light in the irradiated capillary accounts for almost 40% of the total light, while the amount in it and its adjacent two capillaries account for 80% of the total amount of light; meanwhile, the light in the six capillaries, including the irradiated capillary and its adjacent five capillaries, accounted for 95% of the total light. Meanwhile, for the same number of capillaries as mentioned above (1, 3, and 6), the amount of light for 1.25 MeV gamma radiation was 24%, 57%, and 81% of the total light, respectively. In the simulation, the interaction between the 14.0 MeV neutrons and the ^{12}C nucleus was not considered. The heavy charged particles gain less kinetic energy from neutrons and produce less light than the recoil protons with the same energy, which are deposited around the interaction spot. The result from Ref. 8 shows that more than 90% of the light output of an incident neutron beam is generated by recoil protons. As the range of electrons produced in the EJ309 scintillator and cladding material by the 1.25 MeV gamma radiation is greater than that of the protons produced by the 14 MeV neutron beam, the distribution of the deposited energy of the electrons extends further. In comparison with electrons, protons are prone to deposit their energy only in adjacent capillaries.[17]

Furthermore, based on Eqs. (1)–(4), the MTF curve can be determined. The curves in the right panel of Fig. 6 represent the MTF results of the LSCA. As expected, the value of the MTF for 14 MeV neutrons is larger than that for 1.25 MeV gamma radiation. The spatial resolution for 14 MeV neutrons

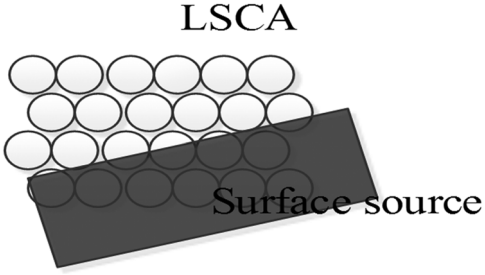

FIG. 4. Model for the simulation of the *ESF*.

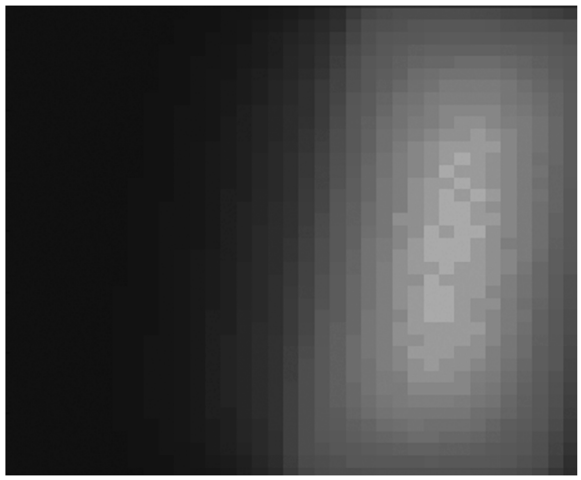

FIG. 5. Simulated ESF image (1.25 MeV gamma).

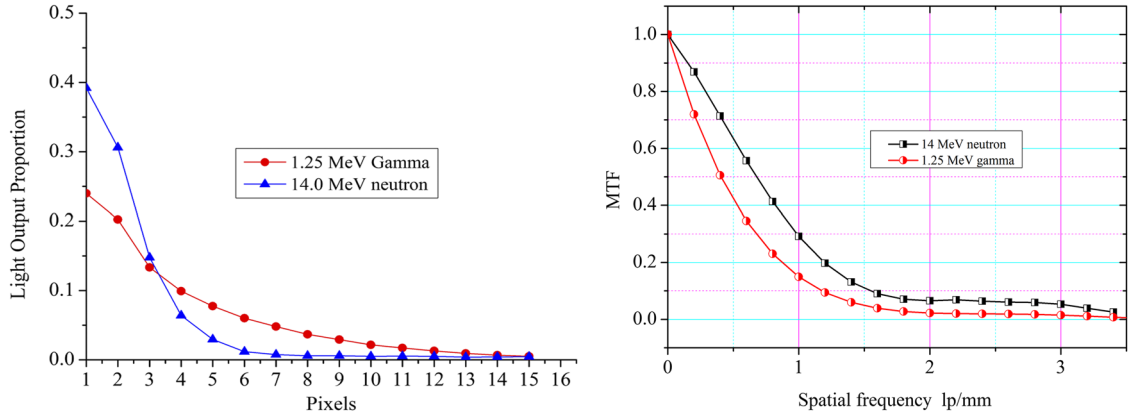

FIG. 6. Amount of light in every capillary (left) and simulated MTF curve (right).

is about 1.6 lp/mm (MTF = 0.1). This result is comparable to that in Ref. 8. For 1.25 MeV gamma radiation, the spatial resolution was 1.1 lp/mm (MTF = 0.1).

C. Experimental measurement of the MTF

The experiment was implemented at a ^{60}Co source facility with an activity of about 4000 Ci. The average energy of the gamma radiation emitted was 1.25 MeV, and the diameter of the ^{60}Co source was 20 mm. A Canon EF 50 mm f/1.2 lens coupled to a model VP-16MC camera was used to register image data. The active image area of this camera was 4872 × 3248 pixels, and the maximum exposure time was 7 s. Prior to the measurements, calibrations of the flat-field radiographs of the array were performed to correct the measurement. To obtain an image with sufficient contrast, the bar target used for measuring the ESF must be thick enough and made of a high atomic number material. A 5-cm-thick tungsten bar with a width of 1 cm was placed on the front of the LSCA. One side of the tungsten block had a curvature with a 1 m radius to minimize misalignment effects. The edge of the tungsten bar with the curvature was sloped at an angle of about 6°, which is the same as mentioned above for the simulation model. The distance between the LSAC and ^{60}Co source was 2.2 m. On the surface of the LSCA, the spatial resolution sampled by a charge coupled display (CCD) imaging system was 0.07 mm. A schematic diagram of the MTF measurement setup is shown in the left panel of Fig. 7. The acquired ESF image was flat-field corrected, and some bright noise spots that were registered when scattered gamma radiation interacted with the

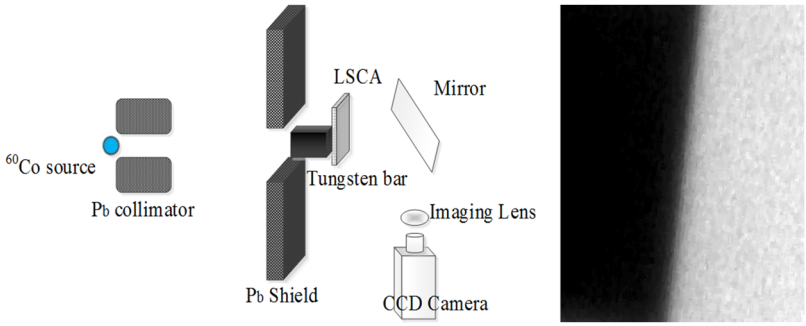

FIG. 7. Schematic diagram of the MTF measurement setup (left) and experimental ESF image (right).

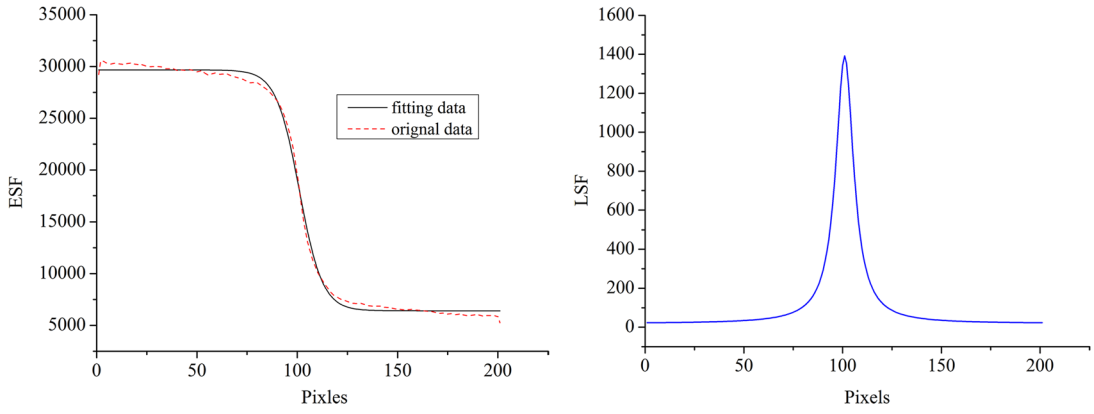

FIG. 8. *ESF* curve (left) and *LSF* curve (right).

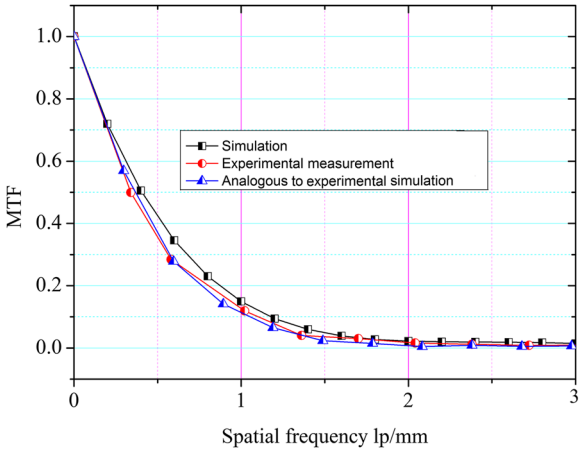

FIG. 9. The simulated and measured MIT curves for the LSCA.

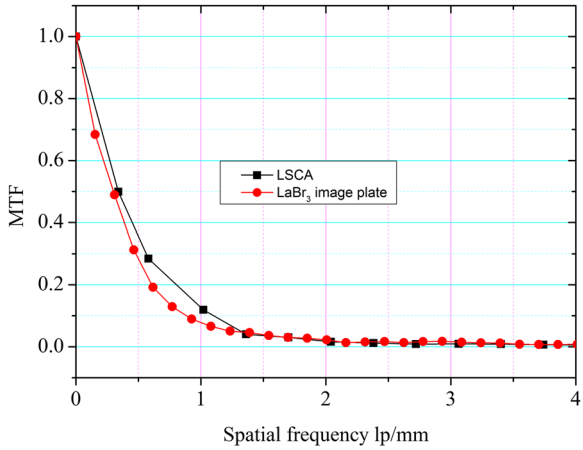

FIG. 10. The experimentally determined MTFs of the LSCA and $LaBr_3$ image plate.

CCD were eliminated. The processed ESF image is shown in the right panel of Fig. 7.

The ESF and LSF curves were obtained from the ESF image acquired using the method described in the first part of Sec. III; the ESF and LSF curves are shown in Fig. 8 (left and right panels, respectively). The full width at half maximum of the LSF curves spans 10 CCD pixels (about 0.7 mm).

Taking the Fourier transform of the LSF yielded the MTF. In Fig. 9, the curves with the legends "simulation" and "analogous to experimental simulation" are both simulation results. The former is a simulated result based on the model shown in Fig. 4 in Sec. III. The latter was obtained from a simulation according to the scheme used for the experimental measurement, as shown in Fig. 7 (the only differences being the mirror and CCD camera). As shown in Fig. 9, the values of the MTF marked "simulation" were greater than those of the measurement. We propose that in the experiment the ^{60}Co source is not a perfect point source and that its geometric dimensions decrease the measured value of the MTF. The curve marked "analogous to experimental simulation" is closer to the experimental results. The curves in Fig. 10 are the experimentally

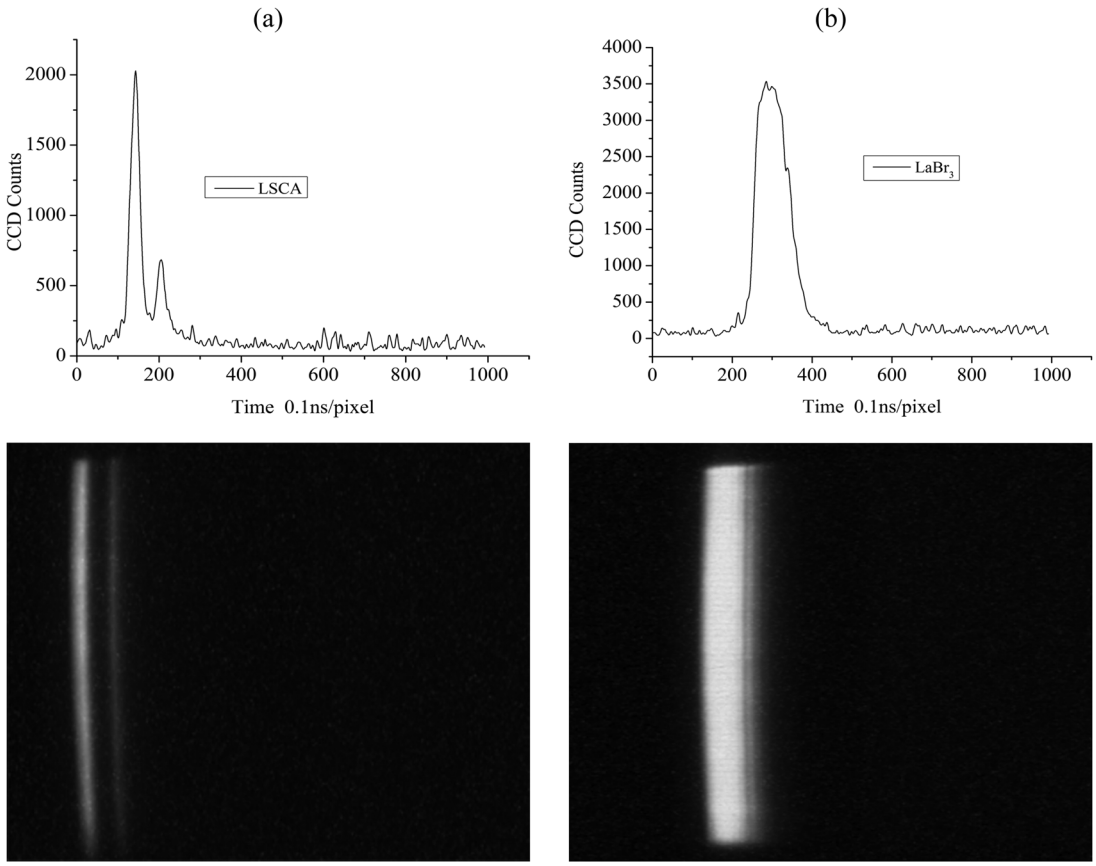

FIG. 11. Measurement over time for the pulsed gamma radiation (a) using the LSCA with the streak camera and (b) using the $LaBr_3$ plate with the streak camera.

determined MTFs of the LSCA and 6-mm-thick $LaBr_3$ image plate. In this comparison, the LSCA shows a better spatial resolution than the $LaBr_3$ image plate. The diameter of the $LaBr_3$ image plate was 96 mm.

IV. PRELIMINARY TEST OF THE LSCA AT A PULSED GAMMA FACILITY

To verify the performance of the LSCA coupled with an ultra-violet streak camera, a preliminary test was conducted at the QiangGuang-I facility with pulsed gamma radiation. The duration of each radiation pulse was about 30 ns, and the energy of the gamma rays ranged from 0 to 3.5 MeV. The average energy was about 1.0 MeV. The radiation dose rate at the position of the LSCA was 10^9 rad/s. For comparison, the $LaBr_3$ image plate was placed at the same position as the LSCA. An ultra-violet lens coupled streak camera was used to record the scintillator luminescence. The customized steak camera was designed and developed by the Xi'an Institute of Optics and Precision Mechanics. Its spectral responsivity ranged from 300 to 500 nm, and its maximum temporal resolution was 0.1 ns. Figure 11 shows the accumulated measurement results over the entire duration of the pulsed gamma field, as recorded by the streak camera. In Fig. 11, panels (a) and (b) show the results from the LSCA and $LaBr_3$ image plate, respectively. The upper curves show the intensity distributions for a row of pixels from the gray-scale images below; in the gray-scale images, the horizontal axis represents the time, while the vertical axis represents the intensity scale. In Figure 11(a), a double pulse of radiation was captured. The same result was obtained using an ultrafast pin diode detector. The superior temporal resolution with the LSCA is readily apparent. The gray values in both images reveal that the sensitivity of the LSCA was about 0.57 times that of the $LaBr_3$ image plate when coupled with the same streak camera.

V. CONCLUSION

Important properties of a liquid scintillator capillary array were studied experimentally and by using a Monte Carlo simulation. The emission spectrum was measured, and its maximum emission peak was found to be at a wavelength of 426 nm. As expected, the spatial resolution of the LSCA for 14 MeV neutrons was better than for 1.25 MeV gamma radiation. The MTFs measured for the LSCA and $LaBr_3$ image plate show that the LSCA had a better spatial resolution. By coupling the detection systems with a streak camera, they could be tested at a pulsed gamma facility, and the results show that the LSCA has a comparable sensitivity and better temporal resolution than a $LaBr_3$ image plate.

By comparing the results of Monte Carlo simulations and the experimentally obtained MTF, we found that the geometry of the ^{60}Co source has an effect on the experimental MTF; it can cause the measured value to be lower than the simulated MTF value. In addition, we found that the flat-field non-uniformity of the LSCA mainly exists at the border. The luminance from the border is 30% less than that from the center.

ACKNOWLEDGMENTS

The authors would like to acknowledge Fu Li Wei and Ma Yan, researchers at the Northwest Institute of Nuclear Technology of China, and Jie Liu, a staff member of Zheng Yang Optic–Electricity Technology Ltd. of China, for their assistance and support. This work was supported by the National Natural Science Foundation of China and the State Key Laboratory of Intense Pulsed Radiation Simulation and Effect as well as by the Natural Science Foundation of China under Grant No. 11275155. We thank Jim Bailey, Ph.D., from Liwen Bianji, Edanz Editing China (www.liwenbianji.cn/ac), for editing the English text of a draft of this manuscript.

[1]G. A. de Nolfo, S. D. Hunter, L. M. Barbier, J. T. Link, S. Son, S. R. Floyd, N. Guardala, M. Skopec, and B. Stark, Proc. SPIE **6954**, 695404 (2008).
[2]D. Xu and Z. He, Nucl. Instrum. Methods Phys. Res., Sect. A **574**, 98 (2007).
[3]J. S. Huber, W. W. Moses, M. S. Andreaco, and O. Petterson, IEEE Trans. Nucl. Sci. **48**(3), 684 (2001).
[4]T. Ludziejewski, K. Moszynska, M. Moszynski, D. Wolski, W. Klamra, L. O. Norlin, E. Devitsin, and V. Kozlov, IEEE Trans. Nucl. Sci. **42**(4), 328 (1995).
[5]E. V. D. van Loef, P. Dorenbos, C. W. E. van Eijk, K. W. Kramer, and H. U. Gudel, Nucl. Instrum. Methods Phys. Res., Sect. A **486**, 254 (2002).
[6]W. M. Higgins, A. Churilov, E. van Loef, J. Glodo, M. Squillante, and K. Shah, J. Cryst. Growth **310**, 2085 (2008).
[7]J. Blaha, M. Finger, M. Slunečka, M. Šulc, and M. Vognar, Radiat. Meas. **38**, 805–808 (2004).
[8]Q. Jia, H. Hu, F. Zhang, T. Zhang, W. Lv, Y. Zhan, and Z. Liu, IEEE Trans. Nucl. Sci. **60**(6), 4727 (2013).
[9]D. Ress, R. A. Lerche, R. J. Ellis, G. W. Heaton, and D. E. Lehr, Rev. Sci. Instrum. **66**, 4943 (1995).
[10]L. Disdier, R. A. Lerche, J. L. Bourgade, and V. Yu. Glebov, Rev. Sci. Instrum. **75**, 2134 (2004).
[11]S. K. Park, R. Schowengerdt, and M. Kaczynski, Appl. Opt. **23**, 2572 (1984).
[12]S. E. Reichenbach, S. K. Park, and R. Narayanswamy, Opt. Eng. **30**, 170 (1991).
[13]W. Wittenstein, J. C. Fontanella, A. R. Newbery, and J. Baars, Opt. Acta **29**, 41 (1982).
[14]H. Wong, Opt. Eng. **30**, 1394 (1991).
[15]P. W. Wang, Ph.M. dissertation (Northwest Institute of Nuclear Technology, Xi'an, 2003).
[16]X. Cao, H. K. Huang, and A. S. Lou, Proc. SPIE **3977**, 580 (2000).
[17]D. Vartsky, I. Mor, M. B. Goldberg, I. Mardor, G. Feldman, D. Bar, A. Shor, V. Dangendorf, G. Laczko, A. Breskin, and R. Chechik, Nucl. Instrum. Methods Phys. Res., Sect. A **542**(1–3), 206 (2005).